

Finding type and location of the source of cardiac arrhythmias from the averaged flow velocity field using the determinant-trace method

Qi-Hao Li,^{1,*} Enid Van Nieuwenhuysse^{1,2,*} Yuan-Xun Xia,¹ Jun-Ting Pan,³ Mattias Duytschaever,⁴ Sebastien Knecht⁴, Nele Vandersickel², Changsong Zhou,^{5,6,7,1} Alexander V. Panfilov^{2,8,9,†} and Hong Zhang^{1,‡}

¹Department of Physics, Zhejiang University, Hangzhou 310027, China

²Department of Physics and Astronomy, Ghent University, Ghent 9000, Belgium

³Ocean College, Zhejiang University, Zhoushan 316021, China

⁴Cardiology Department, AZ Sint-Jan, Bruges 8000, Belgium

⁵Department of Physics, Centre for Nonlinear Studies and Beijing-Hong Kong-Singapore Joint Centre for Nonlinear and Complex Systems (Hong Kong), Institute of Computational and Theoretical Studies, Hong Kong Baptist University, Kowloon Tong, Hong Kong

⁶Research Centre, HKBU Institute of Research and Continuing Education, Shenzhen 518057, China

⁷Beijing Computational Science Research Center, Beijing 100084, China

⁸Laboratory of Computational Biology and Medicine, Ural Federal University, Ekaterinburg 620002, Russia

⁹World-Class Research Center “Digital bidesign and personalized healthcare,” Sechenov University, Moscow 119146, Russia



(Received 19 May 2021; revised 25 August 2021; accepted 5 November 2021; published 1 December 2021)

Life threatening cardiac arrhythmias result from abnormal propagation of nonlinear electrical excitation waves in the heart. Finding the locations of the sources of these waves remains a challenging problem. This is mainly due to the low spatial resolution of electrode recordings of these waves. Also, these recordings are subjected to noise. In this paper, we develop a different approach: the AFV-DT method based on an averaged flow velocity (AFV) technique adopted from the analysis of optical flows and the determinant-trace (DT) method used for vector field analysis of dynamical systems. This method can find the location and determine all important types of sources found in excitable media such as focal activity, spiral waves, and waves rotating around obstacles. We test this method on *in silico* data of various wave excitation patterns obtained using the Luo-Rudy model for cardiac tissue. We show that the method works well for data with low spatial resolutions (up to 8×8) and is stable against noise. Finally, we apply it to two clinical cases and show that it can correctly identify the arrhythmia type and location. We discuss further steps on the development and improvement of this approach.

DOI: [10.1103/PhysRevE.104.064401](https://doi.org/10.1103/PhysRevE.104.064401)

I. INTRODUCTION

Nonlinear waves occur in various chemical and biological excitable media such as the Belousov-Zhabotinsky (BZ) reaction [1,2], the oxidation of CO on platinum [3], aggregations of the *Dictyostelium discoideum* amoebae [4], and other biological and chemical systems. The most important practical application of such waves are the electrical waves of excitation in the heart, which are responsible for cardiac contraction [5]. Abnormal propagation of such waves result in life threatening cardiac tachycardia and fibrillation [6,7].

In most cases, abnormal cardiac excitations occur from abnormal sources of the waves, which can be subdivided into two main classes [8]: focal activity, i.e., when waves periodically originate from a certain region producing target wave patterns; and rotational activity which can occur as the rotation of electrical waves around an inexcitable obstacle in the cardiac tissue or as rotating spiral waves in tissue without obstacles. Finding the location of such sources in the heart

and their classification is an important problem, because it determines the treatment strategy for patients.

Focal and rotational sources of excitation are not unique for heart tissue and also occur in other types of excitable media such as in the BZ reaction as well as in the morphogenesis of *Dictyostelium discoideum*. However, in these excitable media, the source can easily be identified visually. This differs significantly in clinical settings. During ablation procedures, a mapping catheter is placed in the heart via the blood vessels and the excitation wave is recorded with a single or several electrodes. In the case where the patient suffers an atrial periodic arrhythmia (e.g., atrial tachycardia), multiple cycles can be recorded and the excitation pattern of the patient can be visualized properly. However, in the case of more severe and life threatening arrhythmias (e.g., ventricular tachycardia or atrial fibrillation), this spatial resolution cannot be acquired due to the complexity of the waves: they are no longer periodic. Also, for most dangerous arrhythmias, data acquisition of the excitation wave is not only challenging and time consuming, but might not even be possible.

Hence one of the challenges in clinical practice is to identify and classify the sources within low resolution data. Although several methods to find abnormal wave sources have been proposed [9–15], the authors in [16] conclude that

*These authors contributed equally to this work

†Corresponding author: Alexander.Panfilov@UGent.be

‡Corresponding author: hongzhang@zju.edu.cn

further development of such methods remains an important problem, especially development for methods to identify cardiac sources in low resolution recordings.

In this paper, we develop and apply a different method to this problem. The method is based on the calculation of the averaged flow velocity adopting optical flow techniques [17] and further analysis of the averaged velocity field using the method of identification of a critical point in dynamical systems from the reconstructed Jacobian matrix [18]. We refer to this method as the AFV-DT method (averaged flow velocity–determinant-trace method). We illustrate the application of this AFV-DT method for *in silico* generated data for all main types of excitation: focal activity, spiral waves, and waves rotating around an obstacle. From these simulations, we generate ultralow spatial resolution data based on the recordings of the transmembrane potential in these corresponding 8×8 spatial locations (these are thus electrodes). Such spatial resolution is widely used in clinical practice [19,20]. We apply our method to these data sets and study its performance in normal conditions and with added noise. The method finds locations and determines types of excitation sources efficiently and accurately. Finally, we apply our method to two clinical data sets. We show that our method is able to identify the location and source based on the local activation times (LATs) for two patients with atrial tachycardia.

II. METHODS

A. Ionic model

We considered electrical waves generated by the Luo-Rudy model [21]:

$$\frac{\partial V}{\partial t} = -\frac{I_{\text{ion}}}{C_m} + \nabla \cdot (D\nabla V) \quad (1)$$

where V is the transmembrane potential, $C_m = 1 \mu\text{F}/\text{cm}^2$ is the membrane capacitance, $D = 0.001 \text{ cm}^2/\text{ms}$ is the diffusion current coefficient, I_{ion} are the total ionic currents and are determined by ionic gates, whose gating variables are obtained as the solutions to a coupled system of nonlinear ordinary differential equations, and the parameters are simplified as in [22]. The Luo-Rudy model was integrated on a $6 \text{ cm} \times 6 \text{ cm}$ (800×800 grid) medium using the Euler method and only the center region $3.5 \text{ cm} \times 3.5 \text{ cm}$ (466×466 grid) was considered for further analysis. The space and the time steps are $dx = 0.0075 \text{ cm}$, $dy = 0.0075 \text{ cm}$ and $dt = 0.00125 \text{ ms}$, respectively.

Spatial distributions of the membrane potential V are shown in Figs. 1(a) and 2(a) for focal activity and a spiral wave, respectively. The resulting membrane potential is used to record the 8×8 grid within our computational domains. In numerical simulation, the spatial resolution of our grid is $75 \mu\text{m} \times 75 \mu\text{m}$, but such an 8×8 grid corresponds to the current resolution of panoramic basket catheters which can cover the majority of atrial tissue with a spatial resolution of 5 mm [20,23]. We find that the typical wavelength of a spiral wave in our model is $\lambda = 23.3 \text{ mm}$, and with such

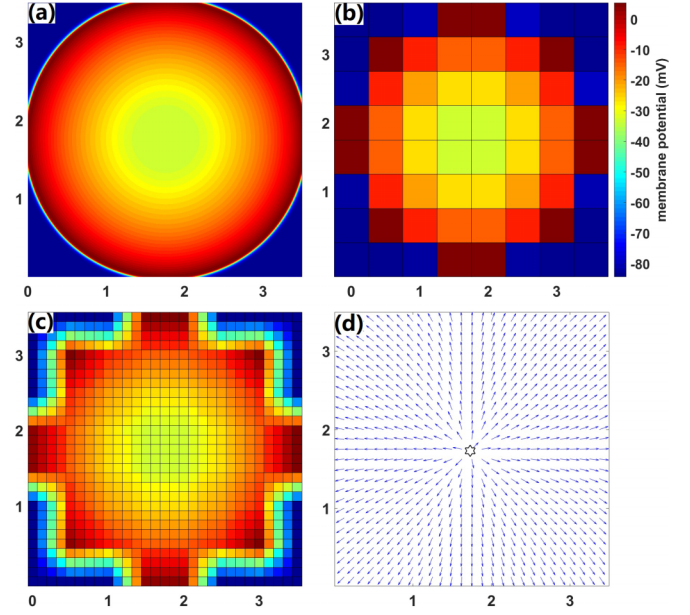


FIG. 1. Localization of a focal source using our AFV-DT method on the simulation in the Luo-Rudy model with $\bar{G}_{Na} = 16$, $\bar{G}_K = 0.423$, $\bar{G}_{Si} = 0.02$. (a) A snapshot of the spatial distribution of the transmembrane potential V . (b) The spatial resolution of V is decreased to the 8×8 grid. (c) The spatial resolution of (b) is increased to a 29×29 grid, by means of a bilinear interpolation protocol. (d) The flow velocity \tilde{C} of the potential V , where the time delay is set to $\delta t = 10 \text{ ms}$ and $\alpha = 6.4$. The white hexagon denotes the focal source where $\tilde{C}_x = 0$ and $\tilde{C}_y = 0$ (see Table I). Model parameters are the same as in Fig. 3 of [22].

wavelength, the resolution of our 8×8 grid is $0.22\lambda \times 0.22\lambda$. These 8×8 grid data are shown in Figs. 1(b) and 2(b), and the membrane potential in the 8×8 grid is equal to the corresponding grid's membrane potential in the high resolution simulation. The 8×8 grid data is interpolated to the 29×29 grid before running calculations, which are shown in Figs. 1(c) and 2(c) and will be discussed later.

B. Time averaged flow velocity: Main equations

The flow velocity was calculated by adopting optical flow techniques originally developed in computer vision [17]. We assume that on a spatial 2D grid (x, y) , we know the values of the variable V at each time t , which we denote as $V_{i,j,k}$, where i, j denote x, y space directions and k denotes the time direction, respectively. Similarly, $V_{i,j,k+\delta}$ denotes the variable V in the subsequent time $t + \delta t$. δt is the time delay between $V_{i,j,k}$ and $V_{i,j,k+\delta}$. If there was an obstacle or an inexcitable region inside the two-dimensional (2D) domain to which waves do not propagate, we assume that for all spatial points (i, j) inside this region and for all time k , $V_{i,j,k} = V_{\text{obs}}$, where $V_{\text{obs}} = \text{const}$ is a parameter which will be defined and discussed later. Based on values $V_{i,j,k}$ and $V_{i,j,k+\delta}$, we calculate averaged gradients using the equations

$$\begin{aligned} \partial_x V_{i,j,k} \approx & \frac{1}{4}(V_{i+1,j,k} - V_{i,j,k} + V_{i+1,j+1,k} - V_{i,j+1,k} \\ & + V_{i+1,j,k+\delta} - V_{i,j,k+\delta} + V_{i+1,j+1,k+\delta} - V_{i,j+1,k+\delta}), \end{aligned} \quad (2a)$$

$$\begin{aligned} \partial_y V_{i,j,k} \approx & \frac{1}{4}(V_{i,j+1,k} - V_{i,j,k} + V_{i+1,j+1,k} - V_{i+1,j,k} \\ & + V_{i,j+1,k+\delta} - V_{i,j,k+\delta} + V_{i+1,j+1,k+\delta} - V_{i+1,j,k+\delta}), \end{aligned} \quad (2b)$$

$$\begin{aligned} \partial_t V_{i,j,k} \approx & \frac{1}{4}(V_{i,j,k+\delta} - V_{i,j,k} + V_{i,j+1,k+\delta} - V_{i,j+1,k} \\ & + V_{i+1,j,k+\delta} - V_{i+1,j,k} + V_{i+1,j+1,k+\delta} - V_{i+1,j+1,k}). \end{aligned} \quad (2c)$$

We substitute these values into the following iterative equations for the velocity $\mathbf{C}_{i,j,k} = (C_x, C_y)_{i,j,k}$ of each grid point through the optical flow method:

$$C_x^{n+1} = \bar{C}_x^n - \partial_x V (\bar{C}_x^n \partial_x V + \bar{C}_y^n \partial_y V + \partial_t V) / [\alpha^2 + (\partial_x V)^2 + (\partial_y V)^2], \quad (3a)$$

$$C_y^{n+1} = \bar{C}_y^n - \partial_y V (\bar{C}_x^n \partial_x V + \bar{C}_y^n \partial_y V + \partial_t V) / [\alpha^2 + (\partial_x V)^2 + (\partial_y V)^2], \quad (3b)$$

where n is the iterative number, and we set $\mathbf{C}_{i,j,k}^0 = 0$ as the initial value, and

$$\begin{aligned} \bar{\mathbf{C}}_{i,j,k} = & \frac{1}{6}(\mathbf{C}_{i-1,j,k} + \mathbf{C}_{i+1,j,k} + \mathbf{C}_{i,j-1,k} + \mathbf{C}_{i,j+1,k}) \\ & + \frac{1}{12}(\mathbf{C}_{i-1,j-1,k} + \mathbf{C}_{i+1,j-1,k} + \mathbf{C}_{i-1,j+1,k} + \mathbf{C}_{i+1,j+1,k}). \end{aligned} \quad (4)$$

α is a weighting factor to prevent noise in the estimated derivatives and is normally proportional to the except noise in the estimate of $\sqrt{(\partial_x V)^2 + (\partial_y V)^2}$ [17]. In simulations, we calculate α in the following way. At each time step k' we calculate $\alpha_{k'}$ as twice the average value of $\sqrt{(\partial_x V)^2 + (\partial_y V)^2}$ in all grid points. We then find α as the average value for one period of spiral waves or focal activity:

$$\alpha = \frac{1}{N} \sum_{k'=1}^N \alpha_{k'}, \quad (5)$$

where $N = T/\Delta t$ and T is a period of waves. The α is determined as a parameter in the iteration processes before calculating the vector field. According to the catheter electrodes sampling frequency 1 kHz [24], the time intervals for recording data are $\Delta t = 1$ ms in all figures.

C. Time averaged flow velocity: Data flow

Before iterating, the data have to be preprocessed. In most of the examples, the data we simulated was recorded on the 8×8 grid, located inside the $3.5 \text{ cm} \times 3.5 \text{ cm}$ area to mimic the spatial accuracy of clinical recording. These 8×8 data $V_{i,j,k}$ were then linearly interpolated to a 29×29 grid. The data are extended to the 31×31 grid (i, j vary from 0 to 30). For that, the boundary layers of 29×29 grid were copied into the corresponding additional layers of the 31×31 grid (the layer 1 of 29×29 grid was copied into the layer 0 of the 31×31 grid, and the layer 29 of the 29×29 grid was copied into the layer 30 of the 31×31 grid). These additional layers are used to impose no-flux boundary conditions used to determine the value of $\partial_x V_{i,j,k}$, $\partial_y V_{i,j,k}$, $\partial_t V_{i,j,k}$, and α through Eqs. (2) and (5).

The iteration procedure starts with Eq. (4) where we set $\mathbf{C}_{i,j,k}^0 = 0$ (i, j vary from 0 to 30), as the initial value, and then we obtain from Eq. (4) that $\bar{\mathbf{C}}_{i,j,k}^0 = 0$. Note that $\bar{\mathbf{C}}_{i,j,k}$ is defined on a grid 29×29 (thus for i, j changing from 1 to 29). Then, $\mathbf{C}_{i,j,k}^1$ is calculated by Eq. (3) also on a grid 29×29 (i, j changing from 1 to 29), based on the value of $\bar{\mathbf{C}}_{i,j,k}^0$, $\partial_x V_{i,j,k}$, $\partial_y V_{i,j,k}$, $\partial_t V_{i,j,k}$, and α .

To calculate the next value of $\bar{\mathbf{C}}_{i,j,k}$ for all 29×29 grids, we use Eq. (4) and extend $\mathbf{C}_{i,j,k}$ to the 31×31 grid (i, j vary from 0 to 30). Calculations for nonboundary elements in Eq. (4) are straightforward. For the calculation of boundary elements, we assume that elements indexed outside the 29×29 grid are equal to the corresponding inner layer elements. For example, if $i = 1$, $\mathbf{C}_{0,j,k}$ equal to $\mathbf{C}_{1,j,k}$. As a result, we obtain the next value of $\bar{\mathbf{C}}_{i,j,k}$, and by substituting it into Eq. (3) and continuing the iteration processes, we get $\mathbf{C}_{i,j,k}^2, \mathbf{C}_{i,j,k}^3, \dots, \mathbf{C}_{i,j,k}^n$. In this paper, we performed $n = 128$ iterations, which were sufficient for the iteration processes to converge. The final value of $\mathbf{C}_{i,j,k}^{128}$ was used as the flow velocity.

If $\mathbf{C}_{i,j,k}$ is located inside the obstacle, it will be initially zero, i.e., $\mathbf{C}_{i,j,k}^0 = 0$. Inside the obstacle $\partial_x V_{i,j,k}$, $\partial_y V_{i,j,k}$, and $\partial_t V_{i,j,k}$ are all equal to zero except at the boundary of the obstacle. Because Eq. (4) will average the vector in the space at each step of the iteration, the value of $\bar{\mathbf{C}}_{i,j,k}$ will be affected by $\mathbf{C}_{i,j,k}$ at the neighboring points ($\mathbf{C}_{i-1,j,k}$, etc.). Thus if $\bar{\mathbf{C}}_{i,j,k}$ is located at the boundary of the obstacle, it will be affected by $\mathbf{C}_{i,j,k}$ outside the obstacle where $\mathbf{C}_{i,j,k} \neq 0$. Therefore, $\bar{\mathbf{C}}_{i,j,k}$ at the boundary inside the obstacle will become a nonzero vector, and in turn $\mathbf{C}_{i,j,k}$ at the boundary inside the obstacle will also become nonzero, etc. After several iterations, the inner obstacle area will form a stable distribution of nonzero $\mathbf{C}_{i,j,k}$. The value of the voltage inside the obstacle $V_{i,j,k} = V_{\text{obs}}$ is a parameter of the algorithm. In most of the cases we use $V_{\text{obs}} = -84$ mV, which is equal to the resting potential in the used model. Later we show that the performance of the algorithm does not depend on the particular choice of V_{obs} .

In general, for velocity calculation from the values of the membrane potential $V_{i,j,k}$ and $V_{i,j,k+\delta}$ at time t and at a subsequent time $t + \delta t$, δt should be in a narrow range, which is often unknown *a priori*: too large or too small δt values will affect the final result. Interestingly, we found that the choice of δt for flow velocity averaged in the range $0.5T - 1.5T$ (in this paper, we chose $1.0T$) using the equation given below is not so essential:

$$\bar{\mathbf{C}}_{i,j,k} = \sum_{k'=k-N/2}^{k+N/2} \mathbf{C}_{i,j,k'}. \quad (6)$$

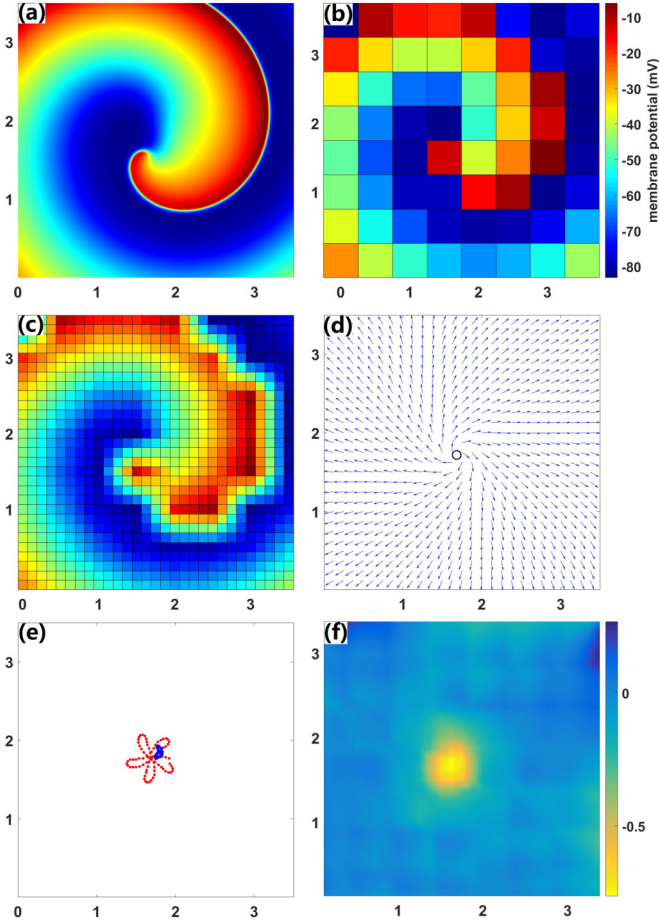


FIG. 2. Localization of the rotation center of a spiral wave using our AFV-DT method. (a) A snapshot of the spatial distribution of the transmembrane potential V . (b) The spatial resolution of V is decreased to a 8×8 grid. (c) The spatial resolution of V is increased to a 29×29 grid by means of a bilinear interpolation protocol. (d) The averaged flow velocity $\tilde{\mathbf{C}}$ of the potential V is shown. The white circle denotes the rotation center of the clockwise spiral, where $\tilde{C}_x = 0$ and $\tilde{C}_y = 0$. (e) The red PS trajectory line is obtained by the modified Jacobian-determinant method with a time delay 2 ms [13] on the high resolution grid. The blue rotation center trajectory is obtained by our AFV-DT method on the low resolution grid. (f) The numerical values of $\nabla \times \tilde{\mathbf{C}} \cdot \hat{\mathbf{z}}$. All other parameters are the same as in Fig. 1.

In this case, the averaged flow velocity does not significantly depend on δt .

The central 27×27 points (2–28) of the averaged flow velocity $\tilde{\mathbf{C}}_{i,j,k}$ were displayed, because the velocity of the boundary layer is unreliable due to the no-flux boundary condition. Examples of the resulting averaged flow velocity are shown in Figs. 1(d) and 2(d) for focal activity and a spiral wave, respectively. All vectors in the figures are normalized.

D. Critical points

Complex waves can be classified around critical points, which are located at the intersection of two contour lines $\tilde{C}_x = 0$ and $\tilde{C}_y = 0$. Each critical point is categorized by using the trace (τ) and the determinant (Δ) of the Jacobian

matrix [18]:

$$J = \begin{pmatrix} \frac{\partial \tilde{C}_x}{\partial x} & \frac{\partial \tilde{C}_x}{\partial y} \\ \frac{\partial \tilde{C}_y}{\partial x} & \frac{\partial \tilde{C}_y}{\partial y} \end{pmatrix}. \quad (7)$$

The symbols used to represent the pattern, the kind of the pattern, and the corresponding determinant-trace conditions are shown in Table I.

III. RESULTS

A. Numerical results for focal activity



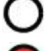


We analyze focal activity in the Luo-Rudy model (1). The waves are generated by the periodic stimulation of a small area (the diameter is 0.5 cm) [25]. The stimulation is performed by the constant current $I_{\text{stim}} = -80 \mu\text{A}/\text{cm}^2$ during 1 ms [26] and the period of stimulation is $T = 100$ ms. Changing the diameter of the stimulated area between 0.1 and 1.0 cm does not affect the results. The spatial distribution of the potential V at a certain moment is shown in Fig. 1(a). In Fig. 1(b), we show the same pattern on a low resolution 8×8 grid, with a spatial resolution of 5 mm. This 8×8 grid data is interpolated onto a 29×29 grid [Fig. 1(c)] on which the averaged flow velocity $\tilde{\mathbf{C}} = (\tilde{C}_x, \tilde{C}_y)$ of the potential V is calculated [Fig. 1(d)]. The white hexagon at the center shows the location of the focal source found by our AFV-DT method. In particular, this is a point where the averaged flow velocity $\tilde{C}_x = 0$ and $\tilde{C}_y = 0$, and the Jacobian matrix at this point satisfies the corresponding conditions on the trace (τ) and the determinant (Δ) ($\Delta > 0$, $\tau^2 > 4\Delta$, $\tau > 0$) (see Table I). The found location of the focal source almost exactly coincides with the true location.

B. Numerical results of spiral waves

We analyze a spiral wave generated by the same parameters as used in Fig. 1. In this case, the spiral wave is meandering with a rotation period of $T = 54.3$ ms. A snapshot of the spatial distribution of the transmembrane potential V is shown in Fig. 2(a). Figure 2(b) shows the same pattern on a low resolution 8×8 grid, with a spatial resolution of 5 mm. These 8×8 grid data are interpolated onto a 29×29 grid [Fig. 2(c)] on which the averaged flow velocity $\tilde{\mathbf{C}} = (\tilde{C}_x, \tilde{C}_y)$ of the potential V is calculated for a time delay of $\delta t = 10$ ms and $\alpha = 12$ ($T = 54$ ms) [Fig. 2(d)]. The white circle at the center shows the location of the rotation center of the clockwise rotating spiral wave found with our AFV-DT method. It is found as a point where the averaged flow velocity $\tilde{C}_x = 0$ and $\tilde{C}_y = 0$, and the Jacobian matrix at this point satisfies the corresponding conditions on the trace (τ) and the determinant (Δ) ($\Delta > 0$, $\tau^2 < 4\Delta$ and $\nabla \times \tilde{\mathbf{C}} \cdot \hat{\mathbf{z}} < 0$) (see Table I).

In Fig. 2(e) we compare the trajectory of the phase singularity (PS) determined by the modified Jacobian-determinant method [13] (the red line), and the trajectory of rotation center determined by our AFV-DT method (the blue line). The red trajectory is obtained on the high resolution 400×400 grid and the blue trajectory on the 8×8 grid. We see that the PS of the spiral wave found on the high resolution data by the modified Jacobian-determinant method [13] is located very

TABLE I. The pattern, kind, and determinant-trace conditions of different complex waves. τ is the trace and Δ is the determinant of the Jacobian matrix, respectively.

Pattern symbols	Kind	Condition
	focal source	$\Delta > 0, \tau^2 > 4\Delta$ and $\tau > 0$
	focal sink	$\Delta > 0, \tau^2 > 4\Delta$ and $\tau < 0$
	rotation center (clockwise)	$\Delta > 0, \tau^2 < 4\Delta$ and $\nabla \times \tilde{\mathbf{C}} \cdot \hat{\mathbf{z}} < 0$
	rotation center (counterclockwise)	$\Delta > 0, \tau^2 < 4\Delta$ and $\nabla \times \tilde{\mathbf{C}} \cdot \hat{\mathbf{z}} > 0$
	saddle	$\Delta < 0$

close to the rotation center of the spiral wave found by our method based on the low resolution data. Figure 2(f) also shows the numerical values of $\nabla \times \tilde{\mathbf{C}} \cdot \hat{\mathbf{z}}$. Here, the sign of $\nabla \times \tilde{\mathbf{C}} \cdot \hat{\mathbf{z}}$ at the rotation center determines the rotation direction of a spiral wave. Namely, if $\nabla \times \tilde{\mathbf{C}} \cdot \hat{\mathbf{z}} > 0$, the spiral wave rotates counterclockwise, while if $\nabla \times \tilde{\mathbf{C}} \cdot \hat{\mathbf{z}} < 0$, the spiral wave rotates clockwise. The data clearly show that the spiral wave rotates clockwise.

C. Numerical results for waves rotating around obstacles

A large class of arrhythmias in the heart are organized by waves rotating around obstacles or heterogeneities, such as complex anatomical structures, blood vessels, and even damaged tissues [7,27–29]. To test how our method performs for such sources, we made simulations of wave propagation in tissue with multiple obstacles that are constructed with no-flux boundary conditions. Figure 3 shows an example of such simulations. The initial conditions for the algorithm are voltage calculated by Eq. (1) in all medium except obstacle and voltage -84 mV inside the obstacle. In this initial state, the partial derivative $\partial_x V_{i,j,k}$, $\partial_y V_{i,j,k}$, $\partial_t V_{i,j,k}$ and velocity $\mathbf{C}_{i,j,k}^0 = (C_x^0, C_y^0)_{i,j,k}$ in Eq. (3) are both equal to zero inside the obstacle. However, Eq. (4) will average the velocity field in the space. In the process of iterating Eq. (3), a nonzero and stable velocity field can also be obtained at the obstacle. We also performed an additional study in which we calculated flow velocity for various values of potentials inside the obstacle (-50 mV, -30 mV, 0 mV). We find that change of potential does not affect the results. In Fig. 3(a), the wave rotates around a 1 cm diameter obstacle. In Fig. 3(b), there are multiple obstacles, and the wave rotates around one of them. Figures 3(c) and 3(d) show the same data on a low resolution 8×8 grid. The averaged flow velocity $\tilde{\mathbf{C}}_{i,j,k} = (\tilde{C}_x, \tilde{C}_y)_{i,j,k}$ of the potential V and location and type of sources found by our AFV-DT method are shown in Figs. 3(e) and 3(f). We see that the location determined by our method is close to the geometric center of the obstacle. When there are multiple obstacles distributed in the tissue, our method correctly identifies the true obstacle around which the rotation occurs.

D. Effect of noise

We also check whether our method is robust against noise [13,14,30]. We add spatiotemporal white noise $\sigma(x, y, t)$ [30] to the right-hand side of Eq. (1) to study the effect of noise on the averaged flow velocity method, in which $\langle \sigma(x, y, t) \rangle = 0$, $\langle \sigma(x, y, t)\sigma(x', y', t') \rangle = \eta\delta(x-x')\delta(y-y')\delta(t-t')$. We use the same parameters in the Luo-Rudy model as those used in Fig. 1 and with $\eta = 0.02$ to generate focal activity and spiral wave. Figures 4(a) and 4(b) are snapshots of the focal activity and spiral wave with spatiotemporal white noise. Figures 4(c) and 4(d) are the one-dimensional spatial distributions of membrane potential V corresponding to the black line in Figs. 4(a) and 4(b), respectively. We see that the wave fronts of focal activity and spiral wave are no longer smooth. Figures 4(e) and 4(f) show the low resolution records on the 8×8 grid. Figures 4(g) and 4(h) show the averaged flow velocities, from which the focal source and the rotation center of the spiral wave were correctly identified using the AFV-DT method.

E. Local activation time

In previous examples, we applied the proposed AFV-DT method on the transmembrane potential of *in silico* data. However, current clinical cardiac mapping systems record electrograms, whose shapes substantially differ from transmembrane voltage. From these electrograms recorded at multiple locations on the endocardial surface, clinical systems determine the moment of passing of the excitation front at a given location; this is called the local activation time (LAT). Based on the spatial distribution of these LATs, high density activation maps are created and electrophysiologists make a conclusion on the type and location of the arrhythmia based on these technologies. However, as these maps are challenging and operator dependent, we aim for mathematical technologies to overcome these issues. Therefore, to apply our tool to clinical data sets, we needed to modify our AFV-DT method in order to be able to apply it not only on the transmembrane voltage, but also on the distributed LAT data. These adaptations were stepwise illustrated in Fig. 5. At first, based on the spiral wave example from Fig. 2(a), we derived the LATs of the spiral on a low resolution 8×8 grid. The LAT was defined as the time when the wave front arrives at the given electrode location, namely when the voltage at the grid

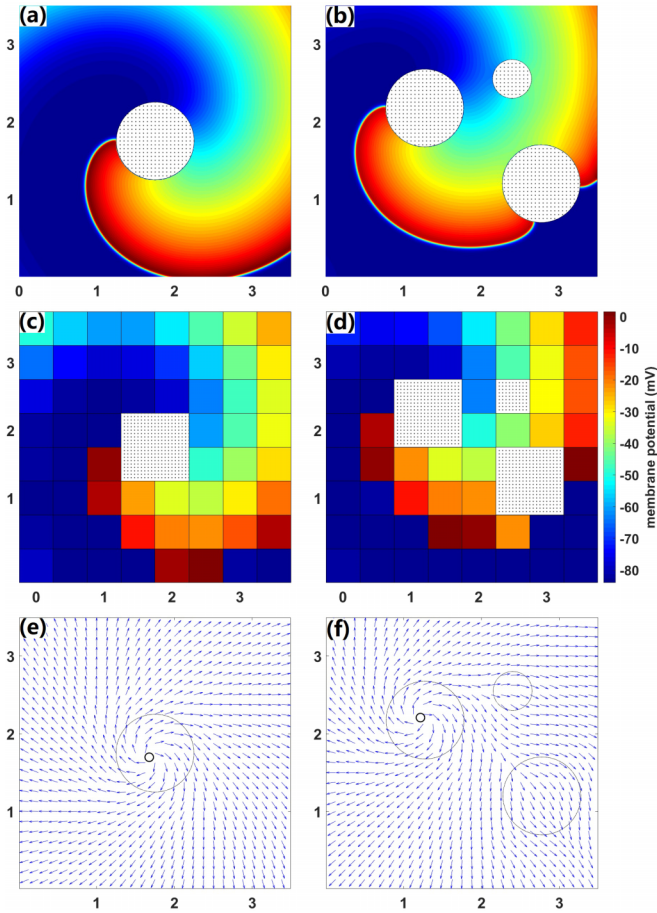


FIG. 3. Localization of the rotation center of the wave rotating around an obstacle using our AFV-DT method. Panels (a) and (b) are snapshots of the spatial distribution of the membrane potential V for waves rotating around a 1 cm diameter obstacle. The dotted parts denote the obstacles. Panels (c) and (d) show the spatial distribution of the membrane potential V on 8×8 grid. (e) The averaged flow velocity \vec{C} . The white circle denotes the rotation center of the clockwise rotating wave, where $\vec{C}_x = 0$ and $\vec{C}_y = 0$. (f) The averaged flow velocity \vec{C} of the rotating wave in tissue with multiple obstacles. The obstacles on the left and the bottom have a diameter of 1 cm and the obstacle on the top have a diameter of 0.5 cm. All other model parameters are the same as in Fig. 1. The period of the rotating wave is $T = 70.6$ ms, the time delay $\delta t = 10$ ms and $\alpha = 10$.

point jumps above -35 mV [22]. As a result we acquired $LAT_1, LAT_2, \dots, LAT_n$ at a certain grid point [Fig. 5(a)]. In addition, there are several factors that might affect the accuracy of LAT detection in realistic situations. Therefore, we also test adding Gaussian noise with different standard deviations $\sqrt{\eta} = 1, 2, 3, 4$ ms on the LATs we detected to simulate LAT variation [14]. This will be the input data of our modified AFV-DT method. Second, based on these LATs, the spatial pattern of the transmembrane voltage was reconstructed. For that we precomputed the dispersion relation of our model. More specifically, we stimulated a 1D cable based on the Luo-Rudy model of different periods T , and for each period we found the corresponding shape of the action potential $V(t)$. Note that for each T , $V(t)$ is a periodic function of t , which has a period T . Starting from this, we could process the LAT

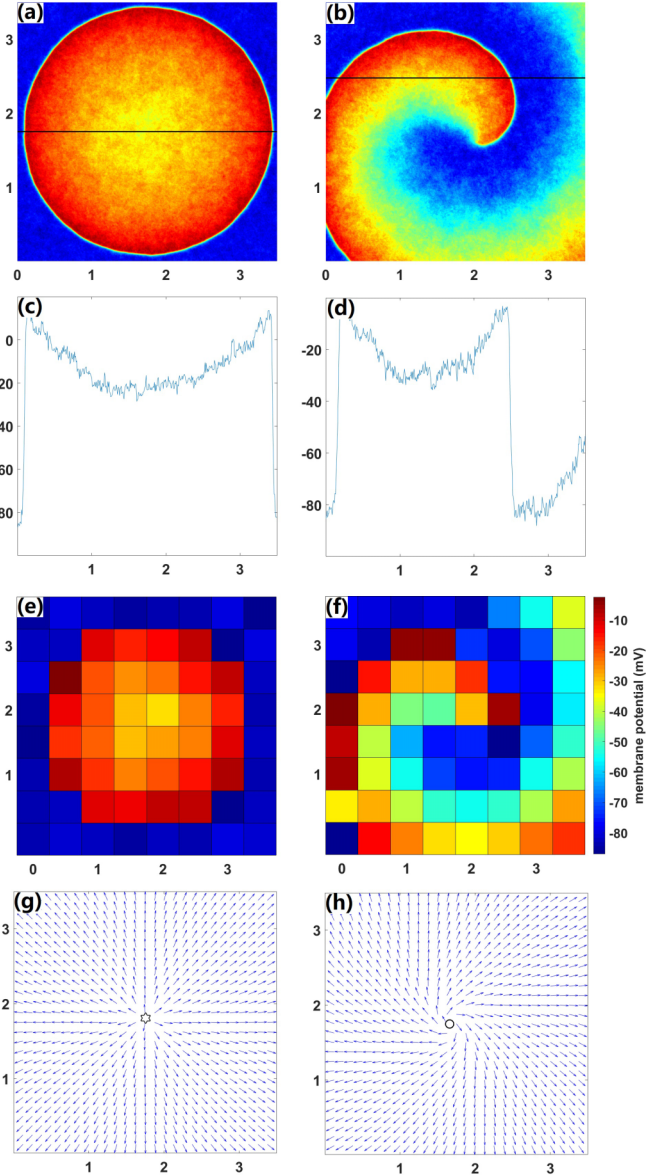


FIG. 4. Localization of the focal source and spiral rotation center of an arrhythmia using our AFV-DT method. Panels (a) and (b) are snapshots of the spatial distribution of the membrane potential V for the focal activity and the spiral wave with spatiotemporal white noise. Panels (c) and (d) are the spatial distribution of the membrane potential V corresponding to the black line in (a) and (b), respectively. Panels (e) and (f) show the spatial resolution of V , decreased to the 8×8 grid. (g) The averaged flow velocity \vec{C} of the focal activity with $\delta t = 10$ ms, $\alpha = 6.8$, and $T = 100$ ms. The white hexagon denotes the focal source. (h) The averaged flow velocity \vec{C} for the spiral wave with $\delta t = 10$ ms, $\alpha = 12.0$, and $T = 54.0$ ms. The white circle denotes the rotation center of the clockwise spiral.

data. First we calculated the time interval between two consecutive LATs as $T_1 = LAT_2 - LAT_1$, $T_2 = LAT_3 - LAT_2 \dots$ and then used the $V(t)$ curve of the corresponding period T_1 to reconstruct the electrical signal between LAT_1 and LAT_2 . Reconstruction of electrical signal was performed as follows. We know the period of the arrhythmia T_1 . Then based on LAT_1 at given location we reconstruct the electrical signal by

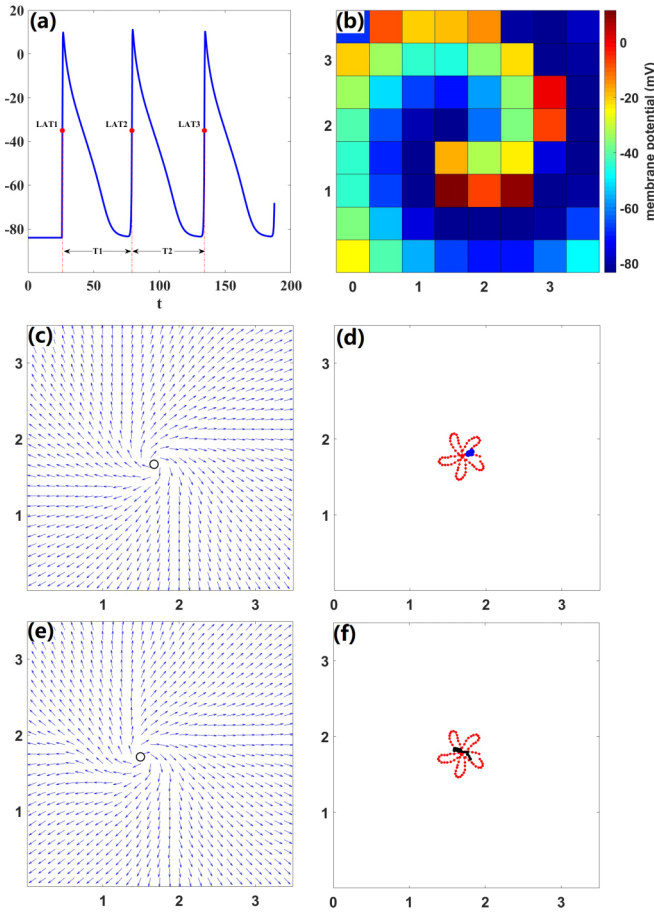


FIG. 5. Localization of the rotation center from LATs using the AFV-DT method. (a) The blue line is the reconstructed electrical signal and the red points are the LATs we detected. (b) A snapshot of the reconstructed electrical signal based on the local arrival time. (c) The averaged flow velocity \bar{C} of a spiral wave ($\delta t = 10$ ms, $\alpha = 12.9$, and $T = 54$ ms) without noise. The white circle denotes the rotation center of the clockwise spiral, where $\bar{C}_x = 0$ and $\bar{C}_y = 0$. (d) The red PS trajectory line is obtained by the modified Jacobian-determinant method with a time delay 2 ms on the original transmembrane potential with a spatial resolution of 400×400 [see Fig. 2(a)]. The blue rotation center trajectory is obtained by the AFV-DT method on the data obtained from the reconstructed electrical signal based on the LAT with a spatial resolution of 8×8 . (e) The averaged flow velocity \bar{C} of a spiral wave ($\delta t = 10$ ms, $\alpha = 13.1$, and $T = 54$ ms) with added Gaussian noise with $\sqrt{\eta} = 4$ ms. (f) The black rotation center trajectory is obtained by using the AFV-DT method on the data obtained from the LATs with added Gaussian noise with $\sqrt{\eta} = 4$ ms.

placing to this point the action potential found in 1D simulations for this period T_1 . We do it in such a way that at this point $V(t) = -35$ mV. As $V(t)$ is a periodic function, the choice of a particular level does not matter. As a result we get the blue line (electrical signal) shown in Fig. 5(a), where the red points show the corresponding LATs. We repeated this algorithm for each grid point and each time interval. Finally, we obtained the spatial distribution of the transmembrane potential [Fig. 5(b)]. Using this spatial dependency we obtained the averaged flow velocity and analyze it using our standard AFV-DT method. The results of this described approach are shown in Figs. 5(c)

and 5(e), and its comparison with the high resolution modified Jacobian-determinant method is shown in Figs. 5(d) and 5(f) [similar to what we did in Fig. 2(e)]. The Gaussian noise added in LAT for Figs. 5(e) and 5(f) is $\sqrt{\eta} = 4$ ms. We see that the AFV-DT method works well on data derived from LATs whether or not noise is added.

IV. DISCUSSION

In this paper, we propose several formulations of the AFV-DT method to find the location of the excitation sources in excitable media. Application of this method to clinical data is the next important step in its development. In this paper, we do not perform extended clinical studies of the AFV-DT method. However, we illustrate below its applicability to two clinical cases of atrial tachycardias.

A. Test of the AFV-DT method on two clinical datasets

We perform an initial test on how the developed AFV-DT method works on clinical data. We apply it to two clinical cases of human atrial tachycardia (AT), a stable periodic atrial arrhythmia. The first presented case is part of the database of AT excitation patterns collected between April and August 2017, for patients undergoing ablation of symptomatic ATs at the AZ Sint-Jan Bruges Hospital (Belgium) [14]. The second case is a single case from another database presented in [31,32]. Data collection in both studies were approved by the local ethics committee of the AZ Sint-Jan Bruges Hospital. The endocardial mapping of these ATs was performed using a single-electrode mapping and ablation catheter with a distal 3.5 mm tip and three 1 mm ring electrodes (THERMOCOOL SMARTTOUCH, Biosense-Webster Inc., Diamond Bar, CA, USA). More details on clinical aspects of two cases used in our study can be found in the Supplemental Material section “Additional information on clinical cases” [33].

In Fig. 6 (the upper row) we present the endocardial electrode mapping of the first patient. The left two pictures show different views of the points where the electrical activity was recorded and they are color-coded by the derived LATs at these electrodes. The Supplemental Material section “Collection and Projection of Clinical data” describes how the data was collected and projected [33]. The right two pictures show the 2D plane projection of the data and their linear interpolation. Figure 6 (lower row) shows the same for the second case.

To test our AFV-DT method for the linear interpolated data of Figs. 6(b) and 6(d) we reconstruct the electrical signal according to the LATs and then analyze the reconstructed electrical signal with our method to find the critical points.

Due to substantial complexity (due to noise) in the clinical data we have to increase the extent of averaging of the data by appropriate choice of α , in order to find the dominating critical point and filter out error points. The sink and saddle will not be displayed in Fig. 7 because they correspond to wave collisions.

We find that the LATs from Fig. 7(a) are generated by focal activity. Our algorithm marked two close locations of this source. For Fig. 7(b) we find that LATs are generated by a wave clockwise rotating around an obstacle. Both findings are

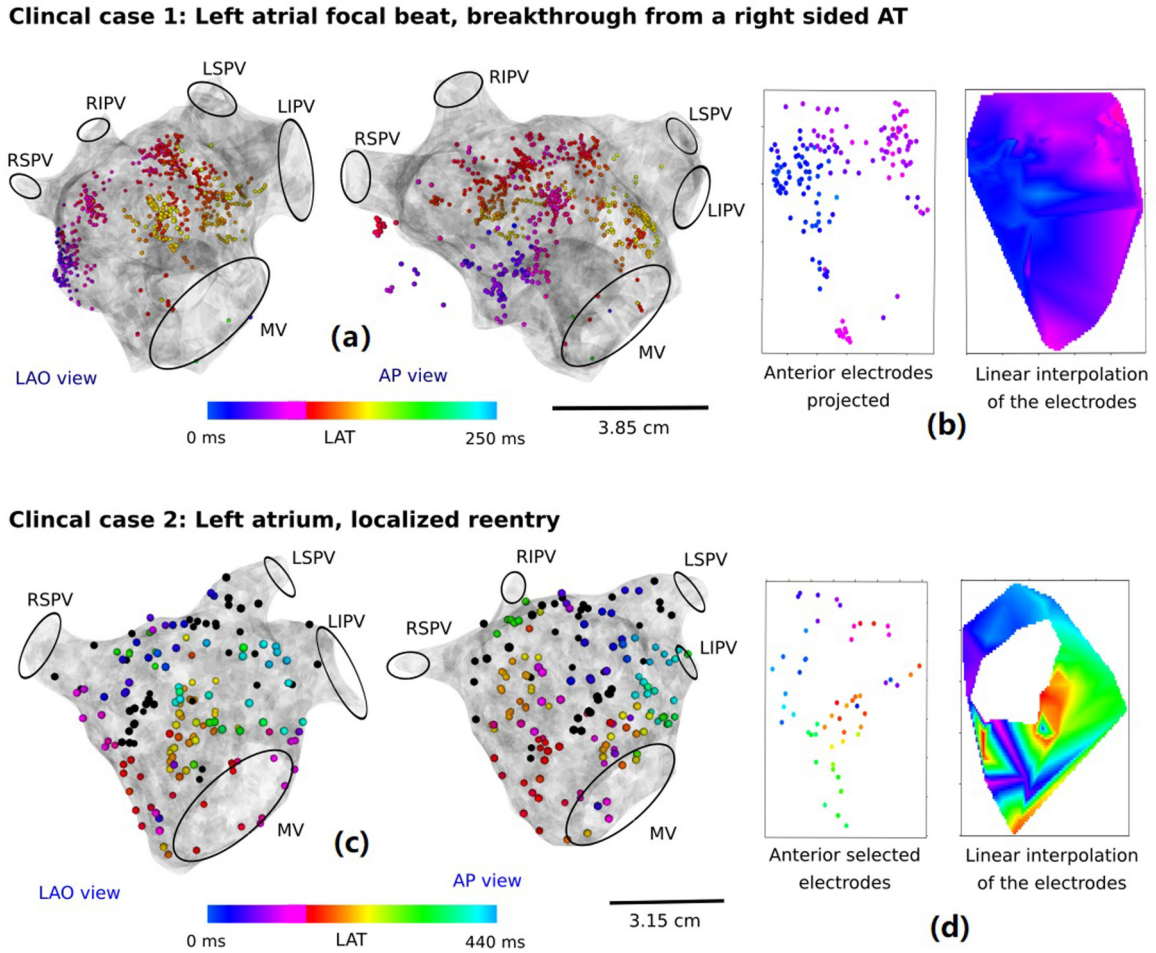


FIG. 6. Clinical recordings of electrical excitation patterns in patients with atrial tachycardia. Panels (a) and (c) show two views of the left atrium obtained from clinical measurements by the CARTO mapping system. The colored points show the locations of the electrodes where electrical activity was recorded. Color represents the activation time at the corresponding electrode locations mapped to the one period of the arrhythmia. The period was 250 ms for case 1 and 440 ms for case 2. Panels (b) and (d) show the projection of the data to the 2D plane and their linear interpolation. The shown landmarks, RSPV and LSPV, are the right superior and left superior pulmonary veins; RIPV and LIPV are the right inferior and left inferior pulmonary veins; MV is the mitral valve. LAO the left anterior oblique view; anterior-posterior view (which are two standard views in the CARTO system).

correct: the type and location of the found sources coincided with clinical findings in these patients. Note that the fact that the algorithm marked two points in Fig. 7(a) reflects that the focal activity here is generated by an extended region and it will not have any consequences for the ablation strategy of this patient. The LAT data presented in Fig. 7(b) do not show clear wave rotation around a scar and even show collision areas in the lower left corner of the picture. However, the AFV-DT method classifies this pattern as rotation. This happened due to extension of vector field inside the obstacle. Note that data for this patient were also analyzed using directed graph (DG) mapping [14,32] and it also classified this source as localized rotation. For that particular patient cardiologists also decided that this is a localized reentry around an anterior scar, and ablation based on that conclusion stopped the arrhythmia. Thus we presume that the case for Fig. 7(b) indeed corresponds to the rotation around the scar and it was correctly identified by the AFV-DT method. Thus we demonstrate that our AFV-DT method was able to determine the type and location of sources organizing cardiac arrhyth-

mias in two clinical cases of patients with nonsustained atrial tachycardia.

B. General discussion of the method: Its limitations and development

In this paper we propose several formulations of the AFV-DT method to find the location of sources of excitation in excitable media. The method has two parts: (1) generation of the averaged flow velocity; (2) analysis of the averaged flow velocity.

In part 1 there are three critical parameters: the time delay δt , the averaged time, and the weighting factor α . The value of the time delay δt and averaged time can vary in a wide range without significantly affecting the results. The weighting factor α has to be adjusted in clinical data to filter out noise and errors. However, as this is the only parameter to be chosen, its adjustment is straightforward. In part 2, the critical points, where velocity equals zero, will be automatically identified and categorized.

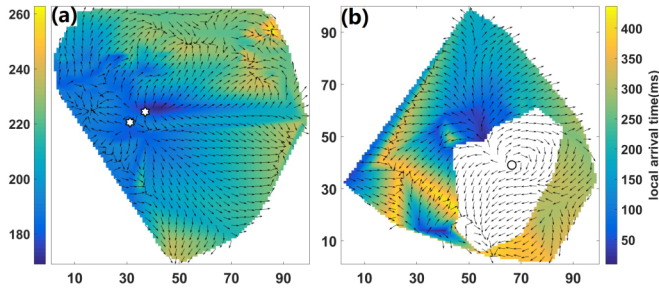


FIG. 7. The background coloring corresponds to the interpolated LATs of the electrical signal. The white region in the second figure corresponds with scar tissue. (a) We show the averaged flow velocity \bar{C} of the focal activity, where the time delay is set to $\delta t = 10$ ms, $\alpha = 50$, and $T = 250$ ms. The white hexagon denotes the source of focal activity. (b) The averaged flow velocity \bar{C} of rotating wave, where the time delay is set to $\delta t = 10$ ms, $\alpha = 50$, and $T = 440$ ms. The white circle denotes the rotation center.

The AFV-DT method is a combination of the averaging technique adopted from the analysis of optical flow [17] and of the determinant-trace method used for classification of equilibrium in theory of dynamical systems [18]. The flow velocity method was used previously for the construction of the velocity field in neuroscience [34]. In these researches, they used different versions of the flow velocity to calculate the velocity field based on phase field of the local field potential, and did not average the velocity field. Using this flow velocity method one can find a vector field showing wave propagation directions. To analyze this vector field we applied the determinant-trace method. A similar method was used in the analysis of spatiotemporal patterns in brain activity [35,36], to categorize the critical points. In this paper we combine both approaches and apply them to characterize electrical activity in cardiac tissue. Using the AFV-DT method we can determine all types of the excitation sources in the heart: focal activity, spiral waves, and waves rotating around obstacles. The important feature of this method is that it is able to find the type of the source in data with a very low spatial resolution; even recording at only 8×8 spatial locations is sufficient. We developed two modifications of the AFV-DT method: one uses the transmembrane voltage as input, and another method uses the LAT at given point as input. In the latter case we reconstructed the transmembrane voltage from the activation times using restitution curves of the model.

We showed that both realizations of the AFV-DT method are robust with respect to noise. Finally, we applied our methodology to two clinical cases of human atrial tachycardia and found that our method can correctly determine the type and location of the sources in clinical datasets. Also as the AFV-DT method works well with transmembrane voltage, it can also be applied to analysis of data obtained using optical mapping of electrical activity of the heart as well [37].

In this paper, the data for transmembrane voltage or local activation times were obtained by using the Luo-Rudy model for cardiac tissue. For the modification of the AFV-DT method to get to the LATs is not necessarily to use the Luo-Rudy model for cardiac tissue and another model can be used to reconstruct the transmembrane voltage. However, as we are

mostly interested in the vector field representing the propagation of the wave front, it would be good to use a model which has a sufficiently steep upstroke and a gradual monotonic repolarization phase of the action potential, to avoid possible errors in the vector field direction due to the shape change. We have also tried the FitzHugh-Nagumo model [38,39] to reconstruct the voltage from the LAT patterns shown in Fig. 5. The results presented in the Supplemental Material section “Voltage reconstruction with different model” [33] show that this model can also properly reproduce the velocity fields of the excitation pattern.

The main aim of our paper is to propose another method to determine the location and type of the sources in excitable media which can work for low spatial resolution data. In recent years there has been fast progress in cardiac mapping techniques for electroanatomical mapping of the heart during arrhythmia. These methods allow collection of information at a large number of spatial points in a short period of time. For example, using the RHYTHMIA system is possible to map arrhythmia at more than 10 000 points [40], using AcQMap it is possible to acquire voltage samples at a rate of 150 000 per second [41]. However, methods of automatic analysis of such large datasets were not sufficiently improved. As a result, in complex cases, cardiologists need to use methods of identification of the arrhythmias, for example, pacing maneuvers, such as PPI-TCL [42], which require substantial time. The methods of automatic analysis of clinical recordings, such as phase mapping [6,43], DG mapping [14,32], and the AFV-DT method developed in our paper may help to overcome this shortcoming and result in more effective ways of management of cardiac arrhythmias in the operation room. We do not want to claim at this stage that our method is better or worse than other existing methods, such as phase mapping or DG mapping. The direct comparison of the AFV-DT method with phase mapping and DG mapping is definitely the most important next step which has to be done in the future. We think, however, that before such comparison additional studies involving the AFV-DT method must be performed. This is because both phase mapping and DG mapping methods were already investigated on large data sets and in many different situations. We think that the AFV-DT method should be applied to more examples of clinical data, studied using different models for cardiac cells, and applied not only for isotropic but also for anisotropic cardiac tissue, anatomical models of the heart, etc. After that, a full comparison of the AFV-DT method and phase mapping and DG mapping can be properly performed.

V. CONCLUSION

We develop a different approach, called the AFV-DT method, to identify the location and type of sources in excitable media. This method can be applied to the spatial voltage data and to the data on the local activation time of the wave and works in two steps. It first generates the averaged flow velocity field and then analyzes this vector field using the determinant-trace method. As an input the method can use the spatial voltage distribution data, or the spatial data on the local activation times of the wave. As output, the method provides the location and the type of the sources and

determines all important types of sources: focal activity, spiral waves, and waves rotating around an obstacle. The method is robust, as it works with a very low spatial resolution (up to an 8×8 grid) and is stable to added noise. We tested our method on many computational data sets and on two clinical examples of patients with atrial tachycardia and showed that it can correctly determine the type and location of the source of the arrhythmia. The method can be used to analyze excitation patterns in numerical, experimental, and clinical recordings.

ACKNOWLEDGMENTS

This work was supported by the National Natural Science Foundation of China under Grants No. 12075203 and No. 11975194, and research at Sechenov University was financed by the Ministry of Science and Higher Education of the Russian Federation within the framework of state support for the creation and development of World-Class Research Centers “Digital biodesign and personalized healthcare” (Grant No. 075-15-2020-926).

-
- [1] A. T. Winfree, *Science* **175**, 634 (1972).
 - [2] V. K. Vanag and I. R. Epstein, *Science* **294**, 835 (2001).
 - [3] S. Jakubith, H. H. Rotermund, W. Engel, A. V. Oertzen, and G. Ertl, *Phys. Rev. Lett.* **65**, 3013 (1990).
 - [4] S. Sawai, P. A. Thomason, and E. C. Cox, *Nature (London)* **433**, 323 (2005).
 - [5] J. M. Davidenko, A. V. Pertsov, R. Salomonsz, W. Baxter, and J. Jalife, *Nature (London)* **355**, 349 (1992).
 - [6] R. A. Gray, A. M. Pertsov, and J. Jalife, *Nature (London)* **392**, 75 (1998).
 - [7] S. Luther, F. H. Fenton, B. G. Kornreich, A. Squires, P. Bittihn, D. Hornung, M. Zabel, J. Flanders, A. Gladuli, L. Campoy, E. M. Cherry, G. Luther, G. Hasenfuss, V. I. Krinsky, A. Pumir, R. F. Gilmour, Jr., and E. Bodenschatz, *Nature (London)* **475**, 235 (2011).
 - [8] Z. Qu, G. Hu, A. Garfinkel, and J. N. Weiss, *Phys. Rep.* **543**, 61 (2014).
 - [9] J. Beaumont, N. Davidenko, J. Davidenko, and J. Jalife, *Biophys. J.* **75**, 1 (1998).
 - [10] F. Fenton and A. Karma, *Chaos* **8**, 20 (1998).
 - [11] A. N. Iyer and R. A. Gray, *Ann. Biomed. Eng.* **29**, 47 (2001).
 - [12] M.-A. Bray, S.-F. Lin, R. R. Aliev, B. J. Roth, and J. P. Wikswo, Jr., *J. Cardiovasc. Electrophysiol.* **12**, 716 (2001).
 - [13] T. C. Li, D. B. Pan, K. Zhou, R. Jiang, C. Jiang, B. Zheng, and H. Zhang, *Phys. Rev. E* **98**, 062405 (2018).
 - [14] N. Vandersickel, E. V. Nieuwenhuysse, N. V. Cleemput, J. Goedgebeur, M. E. Haddad, J. D. Neve, A. Demolder, T. Strisciuglio, M. Duytschaever, and A. V. Panfilov, *Front. Physiol.* **10**, 1138 (2019).
 - [15] D. R. Gurevich and R. O. Grigoriev, *Chaos* **29**, 053101 (2019).
 - [16] M. J. You, P. Langfield, L. Campanari, M. Dobbs, A. Shrier, and L. Glass, *Chaos* **27**, 093938 (2017).
 - [17] B. K. Horn and B. G. Schunck, *Artif. Intell.* **17**, 185 (1981).
 - [18] S. Strogatz, *Nonlinear Dynamics and Chaos* (Westview, Boulder, 2015).
 - [19] K. Umapathy, K. Nair, S. Masse, S. Krishnan, J. Rogers, M. P. Nash, and K. Nanthakumar, *Circ.: Arrhythmia Electrophysiol.* **3**, 105 (2010).
 - [20] W.-J. Rappel and S. M. Narayan, *Chaos* **23**, 023113 (2013).
 - [21] C. H. Luo and Y. Rudy, *Circ. Res.* **68**, 1501 (1991).
 - [22] Z. Qu, F. Xie, A. Garfinkel, and J. N. Weiss, *Ann. Biomed. Eng.* **28**, 755 (2000).
 - [23] D. Vidmar, S. M. Narayan, D. E. Krummen, and W.-J. Rappel, *Phys. Rev. E* **94**, 050401 (2016).
 - [24] T. Lin, A. Rillig, T. Bucur, A. Metzner, S. Mathew, E. Wissner, P. Wohlmuth, K.-H. Kuck, F. Ouyang, and R. R. Tilz, *Europace* **17**, 1791 (2015).
 - [25] H. Zhang, B. Hu, and G. Hu, *Phys. Rev. E* **68**, 026134 (2003).
 - [26] H. Henry and W.-J. Rappel, *Phys. Rev. E* **71**, 051911 (2005).
 - [27] L. Glass, Y. Nagai, K. Hall, M. Talajic, and S. Nattel, *Phys. Rev. E* **65**, 021908 (2002).
 - [28] F. Xie, Z. L. Qu, and A. Garfinkel, *Phys. Rev. E* **58**, 6355 (1998).
 - [29] A. V. Panfilov and J. P. Keener, *J. Theor. Biol.* **163**, 439 (1993).
 - [30] J. Garcia-Ojalvo and J. M. Sancho, *Noise in Spatially Extended Systems* (Springer, New York, 1999).
 - [31] T. Strisciuglio, N. Vandersickel, G. Lorenzo, E. V. Nieuwenhuysse, M. E. Haddad, J. D. Pooter, M. Kyriakopoulou, A. Almorad, M. Lycke, Y. Vandekerckhove, R. Tavernier, M. Duytschaever, and S. Knecht, *Heart Rhythm* **17**, 211 (2020).
 - [32] E. V. Nieuwenhuysse, T. Strisciuglio, G. Lorenzo, M. E. Haddad, J. Goedgebeur, N. V. Cleemput, C. Ley, A. V. Panfilov, J. D. Pooter, Y. Vandekerckhove, R. Tavernier, M. Duytschaever, S. Knecht, and N. Vandersickel, *JACC Clin. Electrophysiol.* **7**, 936 (2021).
 - [33] See Supplemental Material at <http://link.aps.org/supplemental/10.1103/PhysRevE.104.064401> for more details on clinical data, and a supplemental figure about reconstruction signal to test AFV-DT method with a different model.
 - [34] R. G. Townsend, S. S. Solomon, S. C. Chen, A. N. J. Pietersen, P. R. Martin, S. G. Solomon, and P. Gong, *J. Neurosci.* **35**, 4657 (2015).
 - [35] R. G. Townsend and P. Gong, *PLoS Comput. Biol.* **14**, e1006643 (2018).
 - [36] Y. Liang, C. Song, M. Liu, P. Gong, C. Zhou, and T. Knöpfel, *J. Neurosci.* **41**, 3665 (2021).
 - [37] J. I. Laughner, F. S. Ng, M. S. Sulkin, R. M. Arthur, and I. R. Efimov, *Am. J. Physiol. Heart Circ. Physiol.* **303**, H753 (2012).
 - [38] R. FitzHugh, *Biophys. J.* **1**, 445 (1961).
 - [39] J. Nagumo, S. Arimoto, and S. Yoshizawa, *Proc. IRE* **50**, 2061 (1962).
 - [40] L. Mantziari, C. Butcher, A. Kontogeorgis, S. Panikker, K. Roy, V. Markides, and T. Wong, *JACC Clin. Electrophysiol.* **1**, 411 (2015).
 - [41] A. Grace, S. Willems, C. Meyer, A. Verma, P. Heck, M. Zhu, X. Shi, D. Chou, L. Dang, C. Scharf, G. Scharf, and G. Beatty, *JCI Insight* **4**, e126422 (2019).
 - [42] D. W. Kaiser, J. M. Nasir, L. B. Liem, C. Brodt, K. S. Motonaga, S. R. Ceresnak, M. P. Turakhia, and A. M. Dubin, *Heart Rhythm* **16**, 717 (2019).
 - [43] M.-A. Bray and J. P. Wikswo, *Phys. Rev. E* **65**, 051902 (2002).